Strain Partitioning in a Multi-phase V–Ti–Ni Alloy Containing Superelastic Nano-precipitates

Strain Partitioning in a Multi-phase V–Ti–Ni Alloy Containing Superelastic Nano-precipitates

JACLYN L. CHO and C. CEM TASAN

In $V_{45}Ti_{30}Ni_{25}$ (at. pct), superelastic TiNi and a stable V-rich bcc phase (β) coexist in multiple-phase mixtures with each acting as matrix and precipitate. Through nano-indentation measurements and *in situ* synchrotron and SEM tensile tests coupled with digital image correlation analysis, the phase mixtures are revealed to exhibit similar strain-partitioning behaviors but different dependencies of reverse transformation on strain. These insights on multi-phase plasticity provide hints for improved damage resistance in the presence of a superelastic phase.

https://doi.org/10.1007/s11661-022-06900-1

DEFORMATION and transformation behaviors of individual grains in superelastic alloys are more strongly controlled by boundary constraints from neighboring grains than by the orientation of the parent grain, as strain incompatibilities occur.[1–5] In polycrystalline superelastic TiNi, it has been shown that sub-optimal martensitic variants are formed in some grains, decreasing the transformation strain from its maximum value.[2,6,7] In addition, grain boundaries can serve as obstacles, decreasing the speed of martensitic transformation.[4,8] However, the presence of grain boundaries, as well as the presence of inclusions, can also serve as potential nucleation sites for both the forward and reverse phase transformations.[8,9] The stress concentrations around stiff inclusions, which promote martensite nucleation,[4,6,9] also can promote these inclusions as sites for micro-crack formation.[6,9] Ni_4Ti_3 nano-precipitates, coherent within TiNi, stabilize martensite, reduce apparent transformation strains, and suppress dislocation motion.[6] The introduction of ductile intergranular precipitates in polycrystalline Co–Ni–Al, Cu–Zn–Al, and Cu–Al–Ni can enhance local strain compatibility and strain recovery by accommodating transformation strain, as well as slow crack propagation through plastic deformation.[10]

Here, we investigate a multi-phase $V_{45}Ti_{30}Ni_{25}$ (at. pct) alloy containing a superelastic TiNi phase[11] and a stable Ti-rich β phase combined in multiple-phase mixtures of different fractions and morphologies within the same microstructure. In this alloy, we are able to study the deformation behaviors of both the superelastic phase as a precipitate constrained by a plastically deformable matrix, as well as those between superelastic and plastically deformable matrix phases. V–Ti–Ni alloys are known for their high hydrogen permeability,[12,13] but this particular alloy is designed to exhibit mechanically induced martensitic transformation for its transformation-induced crack closure effect,[11,14] while enabling reverse transformation to prevent accumulation of martensite and consumption of this crack closure capacity. This concept is similar to yttria partially stabilized zirconia ceramics[15] and metallic glass composites,[16] where transforming precipitates enable crack closure.[15,17,18] However, V–Ti–Ni alloys with TiNi precipitates exhibit high workability[19] and limited precipitation strengthening in comparison to alloys of the same composition but with Ni and Ti in solution.[20,21] V alloys with similar Ti-alloying content as the β phase in $V_{45}Ti_{30}Ni_{25}$ can exhibit ultimate elongations of ~ 30 pct,[22] and superelastic TiNi of > 50 pct.[23,24] Thus, the superelastic phase stability can be influenced by the plastic deformation of the constituent phases. To this end, we study $V_{45}Ti_{30}Ni_{25}$ to better understand the co-deformation of each phase mixture present in its microstructure, and the resulting effects on the forward and reverse transformation of TiNi within each phase mixture. Previous investigations have demonstrated that strain partitioning and damage in multi-phase alloys or composites with soft and hard features can be effectively investigated using *in situ* SEM experiments supported by microscopic-digital image correlation (μ-DIC) analysis,[25–27] and/or by *in situ* synchrotron X-ray experiments,[28] which are two main techniques employed here.

$V_{45}Ti_{30}Ni_{25}$ (at. pct) samples were produced through vacuum arc melting and were subsequently hot rolled

JACLYN L. CHO and C. CEM TASAN are with the Department of Materials Science and Engineering, Massachusetts Institute of Technology, 77 Mass. Avenue, Cambridge, MA 02139. Contact e-mail: tasan@mit.edu
Manuscript submitted June 18, 2021; accepted November 6, 2022.

Published online: 06 December 2022

and annealed, following the process described in detail in our prior work.[11] An array of 100 nanoindents were performed with a diamond Berkovich tip, loading at 50 μN/s, holding for 2 seconds at 250 μN, and unloading at 50 μN/s. *Ex situ* tensile tests were performed with a 5kN load cell, while interrupted tests were performed *in situ* within a TESCAN MIRA3 scanning electron microscope (SEM) using a 2kN load cell, and *in situ* at the high-energy beamline ID22 at the European Synchrotron Radiation Facility (ESRF). Local strains were measured by DIC with either speckled paint or a dense silica suspension, following the method in Reference 26. High-resolution secondary electron (SE) and backscattered electron (BSE) micrographs (4096×4096 px^2, 100×100 μm^2 view field) from the *in situ* SEM experiment were analyzed by DIC (GOM Correlate Pro, 30×30 px^2 facet size and 20 px spacing). In all tests, a strain rate of 10^{-3} s^{-1} was used. The synchrotron experiment was performed in transmission mode at 64.9 keV with a 0.25 mm $\times$ 0.25 mm beam size and a 2D detector (100 μm pixel size, 4096×4096 pixels) with a sample-to-detector distance of 551 mm. A LaB_6 calibration standard was used.[29] Using the FIT2D software,[30,31] diffraction patterns were integrated from $\varphi = -7.5$ to 7.5 deg and from $\varphi = 82.5$ to 97.5 deg. After integration into 1D profiles, peaks were fitted with a Gaussian shape. The area fitting error was less than 4 pct for each peak. Reported peak areas were normalized to the largest fit peak area for the reported peak. Lattice strains were calculated through peak shift, calculated against the d-spacings either before deformation (B2) or at first appearance of the phase (B19′), assuming homogeneous strain. The lattice strain, thus, may not reflect any pre-straining from gripping the sample or any strain upon initial formation of B19′.

The $V_{45}Ti_{30}Ni_{25}$ (at. pct) alloy contains multiple phases: (i) β, a bcc phase of composition $V_{83}Ti_{12}Ni_5$ (at. pct)[11] (Figure 1(a), darkest phase), (ii) superelastic TiNi, which transforms from austenitic B2 to martensitic B19′[11] (Figure 1(a), lightest phase), and (iii) a brittle[32] phase with Ti_2Ni-like stoichiometry (which will be referred to as Ti_2Ni throughout this work). Definitive identification between $Ti_4Ni_2(O,C)$[33,34] and Ti_2Ni is not possible through diffraction pattern analysis due to similar lattice parameters.[35,36] The β and TiNi phases exist in phase mixtures in various phase fractions and shape factors (Figure 1(b)): (i) β matrix grains containing a high density of TiNi nano-precipitates (β_m + $TiNi_{nano}$, Figure 1(c1)), (ii) β matrix grains with a lower density of TiNi micro-precipitates (β_m + $TiNi_{micro}$, Figure 1(c2)), and (iii) TiNi grains with a mixture of β nano- and micro-precipitates ($TiNi_m$ Figure 1(c3)).

The uniaxial tension tests in Figure 1(d) reveal a yield stress of 590 MPa (at ~ 0.9 pct strain), an ultimate tensile strength of about 900 MPa, an elongation to fracture of approximately 30 pct, and a superelastic plateau at low strains (ending at the inflection point at 5.8 pct strain and 720 MPa).[11,37,38] Representative force–displacement curves and hardness results from the nano-indentation tests are shown in Figures 1(e) and (f), respectively. We find that $TiNi_m$ is slightly softer than β_m (as measured by nanoindents within the β_m + $TiNi_{micro}$ phase mixture but distanced from $TiNi_{micro}$). The addition of $TiNi_{nano}$, which is closely packed enough for multiple precipitates to be within the indentation plastic zone, increases the hardness of β_m + $TiNi_{nano}$ above that of β_m.

Next, we observe local strain evolution through an *in situ* SEM experiment, using μ-DIC in a representative area (Figure 1(a)). Note that this analysis is not including the maximum strain state, *i.e.*, the point of early fracture resulting from Ti_2Ni (Figure 2(f2)). Figures 2(a) through (c) map the local evolution of normal strain in the tensile direction, ε_{xx}. As might be expected from the similarities in hardness, the strain accommodation between the phase mixtures is relatively homogenous at 1.2 pct (Figure 2(a)), although upon closer inspection, all strain bands (regions categorized by micro-DIC analysis as experiencing the top 5 pct of strain with a minimum area of 0.01 μm^2 and a minimum aspect ratio of 2.5, as evaluated with ImageJ, Figure 2(d)) are found to run primarily through $TiNi_m$ in the direction of maximum shear. The largest visible surface topography and contrast changes are also observed in $TiNi_m$ (Supplementary Figure S-1, refer to electronic supplementary material), indicating dislocation activity or phase transformation. Strain band locations, however, are still impacted by the other phases, as visually explained in Figure 2(e). 90 pct of all categorized micro-DIC strain bands neighbor a $TiNi_m$/β_m phase boundary, and 37 pct of strain bands also a $TiNi_m$/Ti_2Ni phase boundary. No strain bands border only $TiNi_m$/Ti_2Ni phase boundaries, but the influence of the brittle Ti_2Ni,[32] which can be seen to fracture even at 1.2 pct strain, is difficult to consider separately from the neighboring β_m. The homogeneity of strain distribution between phase mixtures is quantified through a strain-partitioning plot (Figure 2(f1)). As suggested from the strain band analysis, the average strain (Table I) of $TiNi_m$ (1.37 pct) is indeed higher than both β_m + $TiNi_{micro}$ (0.94 pct) and β_m + $TiNi_{nano}$ (0.95 pct). In addition, a comparison of the top 5 pct of local strains experienced by each phase mixture confirms that $TiNi_m$ experiences the highest maximum strains.

The standard deviation of the strains is relatively large (Table I), so the statistical significance of the difference in strains between phase mixtures is checked following the method described in the electronic supplementary material. This analysis confirms that $TiNi_m$ accommodates a significantly higher local strain than β_m + $TiNi_{nano}$ or β_m + $TiNi_{micro}$. As the global strain increases to 3.7 pct (Figure 2(b)), the same strain-partitioning trend continues. The apparent difference in the strain partitioning by β_m + $TiNi_{micro}$ and β_m + $TiNi_{nano}$ is, however, not statistically significant. That stated, the strains within β_m + $TiNi_{micro}$ are less homogeneous, as can be seen by the larger standard deviation and by comparing the higher strain ranges (Figure 2(f1)). There is also a large standard deviation of the phase strain of Ti_2Ni, which is attributable to the mixture of high strain facets tracking-fractured regions, low strain facets in the relaxed regions immediately neighboring fractures, and typical elastically deformed grains. Before discussing the

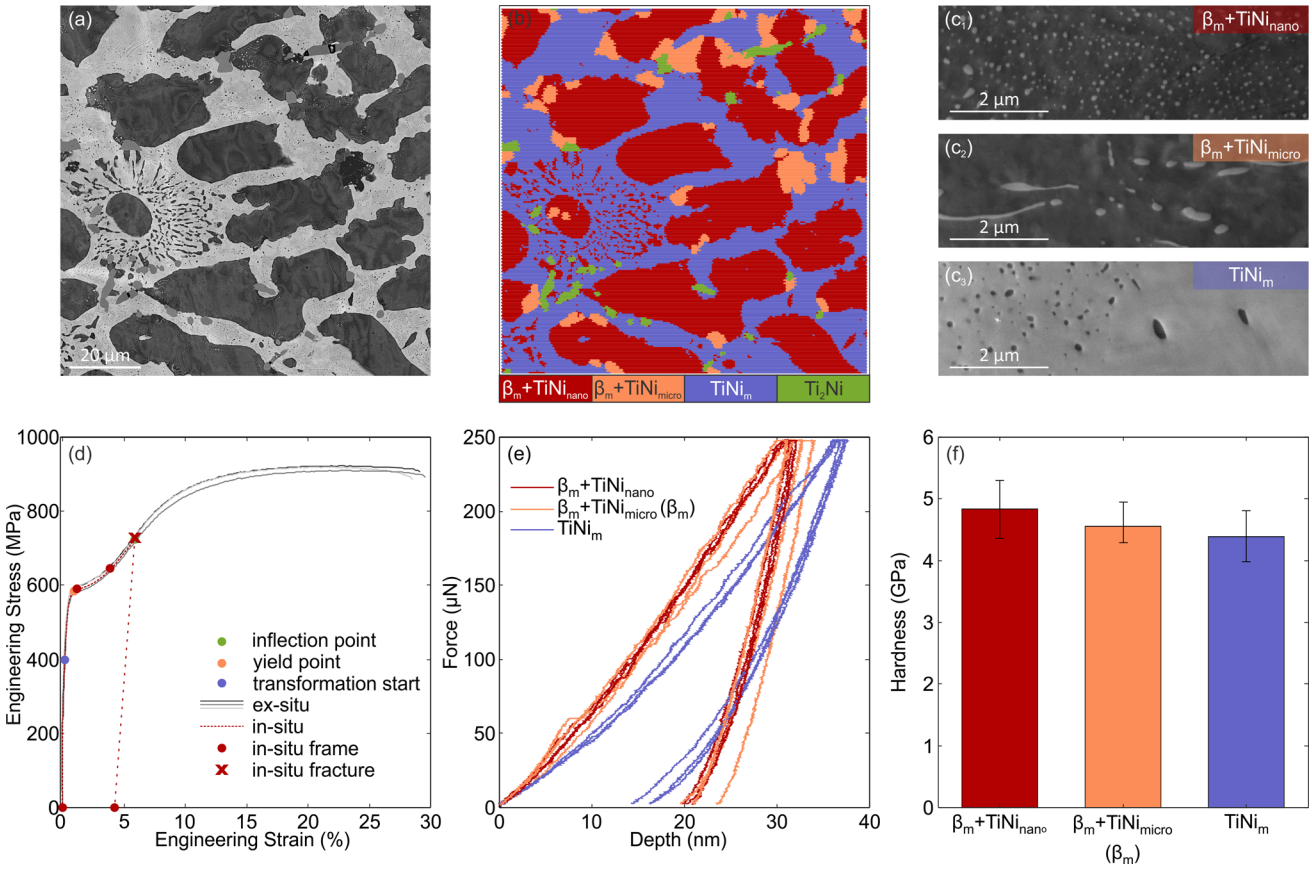

Fig. 1—(*a*) BSE micrograph. (*b*) Map of phase mixtures (with μ-DIC facet resolution) from image processing of BSE image. (c_1) BSE micrograph of β matrix with TiNi nano-precipitates (β_m + $TiNi_{nano}$). (c_2) BSE micrograph of β matrix with TiNi micro-precipitates, (β_m + $TiNi_{micro}$). (c_3) BSE micrograph of TiNi matrix with β precipitates ($TiNi_m$). (*d*) Engineering stress–strain curves from repeated *ex situ* tensile experiments overlaid with points from an *in situ* μ-DIC tensile experiment. (*e*) Sample force–displacement curves from nano-indentation of the β_m + $TiNi_{nano}$ phase mixture, the β_m regions within the β_m + $TiNi_{micro}$ phase mixture, and $TiNi_m$ as shown in (c_1 to c_3). Nano-indents within the β_m + $TiNi_{micro}$ phase mixture only probed the β_m. (*f*) Mean and standard deviation of hardness measured from nano-indentation.

final, post-fracture μ-DIC frame, we carry out a brief assessment of the deformation mechanisms.

As indicated by the surface topography changes (Supplementary Figure S-1) and the plateauing stress at low strain levels (Figure 1(d)), the phase transformation of TiNi from austenitic, cubic B2 into martensitic, monoclinic B19′ is confirmed through *in situ* uniaxial tension experiments with high-energy X-ray diffraction (HE-XRD). Rietveld refinement was not performed due to the complexity of the overlapping diffraction patterns with similar lattice parameters. As such, we select the B2 (100), B19′ (010), and B19′ (100) peaks on which to perform a peak area analysis, as these peaks have minimal overlap with others. There is not a lattice correspondence between them. It should be noted that these are not the peaks with the highest structure factors, and that they are at low 2θ diffraction angles, which when combined with the 2D detector used can lead to peak broadening and lower angular resolution, and thus, lower strain sensitivity. Figure 3(a) shows the peak area development of the B2 (100), B19′ (010), and B19′ (100) peaks. The evolution of these peak areas, normalized to the maximum peak area observed, may be taken as an indication of transformation, but not as a precise phase fraction, as would be obtained through Rietveld refinement. The transformation of B2 → B19′ begins at ~ 400 MPa (0.35 pct global strain). By ~ 6 pct global strain, the transformation appears to be nearly saturated. The B2 lattice strain increases linearly initially, and the rate of increase slows as the rate of phase transformation increases (Figure 3(b)). In contrast, B19′ lattice strain is negligible until a global strain of ~ 4 pct strain, when the majority of B2 has transformed.

A more detailed look at the deformation mechanisms of each phase mixture is obtained from post-mortem SE micrographs from a separate tensile test, where the extent of plastic deformation is quantified by a post-mortem measurement of the reduction in cross-sectional area (RA) (Figure 4). Within β_m + $TiNi_{nano}$ (Figures 4(a1) through (a4)), at low strains (Figure 4(a2)), no slip traces can be seen, but some dislocations can be observed through electron channeling contrast imaging (ECCI) (Figures 4(b1) through (b2)). In the undeformed state, a small number of dislocations are present in proximity to $TiNi_{nano}$ (red arrow, Figure 4(b1)), and dislocation density increases in other locations as strain increases (Figure 4(b2)), indicating that dislocations are pinned at $TiNi_{nano}$ at

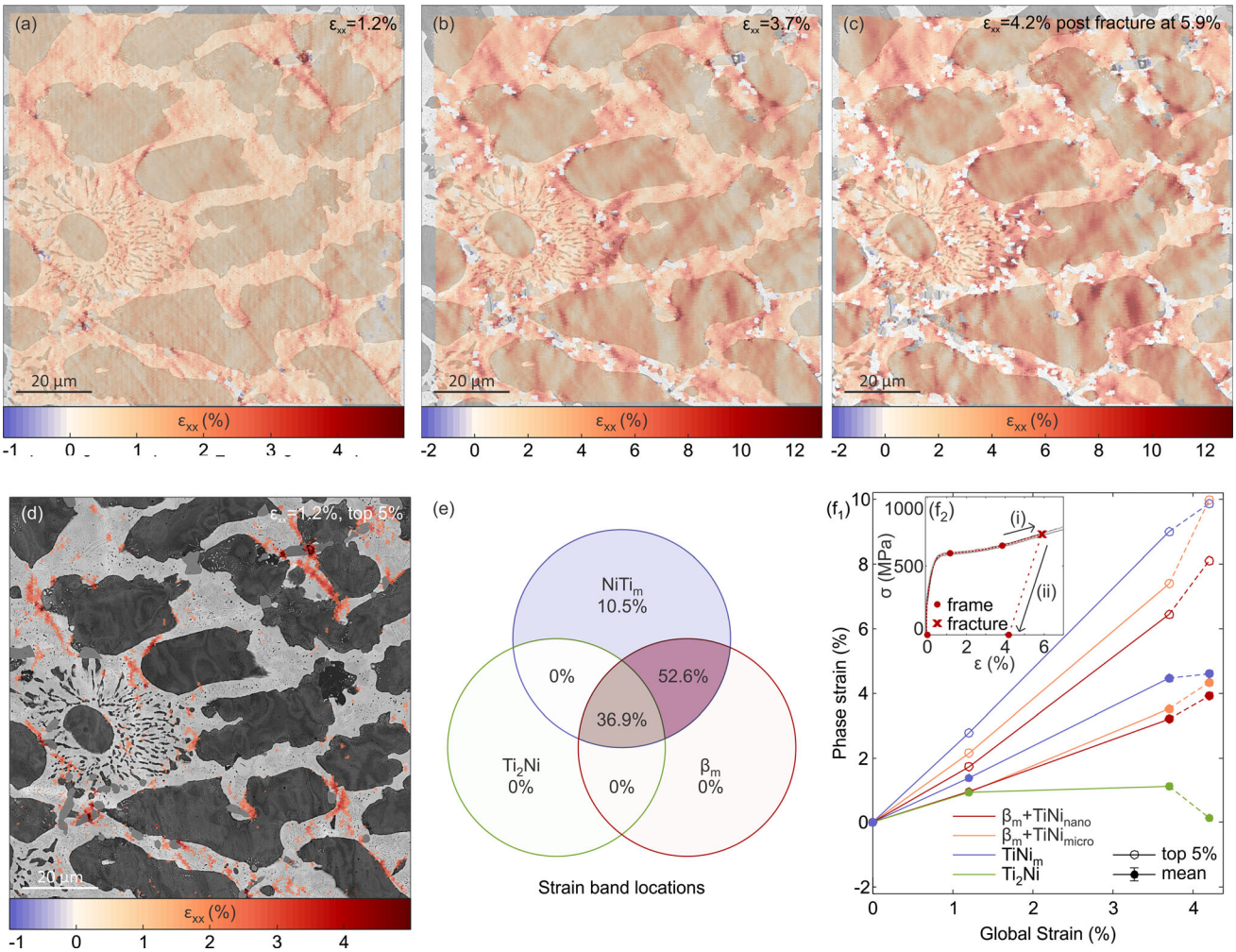

Fig. 2—(*a*) μ-DIC strain map-overlaid BSE micrograph at a global strain of ε_{xx} = 1.2 pct (*b*) Strain map-overlaid BSE micrograph at a global strain of ε_{xx} = 3.7 pct, the last μ-DIC frame before fracture. (*c*) Strain map-overlaid BSE micrograph after fracture, which occurs at ε_{xx} = 5.9 pct. After fracture, the global strain is ε_{xx} = 4.2 pct. (*d*) BSE micrograph with top 5 pct strain bands from (a). (*e*) Percentage of strain bands with an aspect ratio of 2.5 or greater which pass through each matrix phase or combination of matrix phases. (f_1) Strain-partitioning plot showing the mean of the local strains of each type of microstructural region, as well as the means of the 5 pct most strained facets of each type of microstructural region. The dashed lines indicate the change in phase strain after final loading and fracture. (f_2) Engineering stress–strain curves from *in situ* μ-DIC tensile experiment showing the global strains of each analyzed frame and the strain at fracture. Segment (i) indicates the loading portion of the last deformation stage and segment (ii) indicates the post-fracture relaxation portion of the last deformation stage.

low strains. As local strain increases further, wavy surface steps are observed (Figures 4(a3) and (a4)), which often indicates cross-slip.[39] Additionally, most slip traces bypass $TiNi_{nano}$ (Figure 4(b3)). At the highest observed strain levels (~ 22 pct RA, Figure 4(a4)), changes in contrast in a small fraction of $TiNi_{nano}$ are seen (Figure 4(b4)). This is believed to indicate particle shearing, a common progression from dislocation pinning,[40] as martensitic transformation is saturated by ~ 6 pct global strain (Figure 3(a)), while this newly develops at higher strains.

Within β_m + $TiNi_{micro}$, we similarly observe dislocation plasticity (Figures 4(c2) through (c4)) with relatively localized, deep surface features. This appears to be a continuation of the previous trend observed in the *in situ* μ-DIC experiment, where β_m + $TiNi_{micro}$ experiences larger variations of strain than β_m + $TiNi_{nano}$. In $TiNi_m$ (Figures 4(d1) through (d4)), distinct surface steps are formed by 2 pct RA (Figure 4(d2)). In TiNi, surface steps can indicate either B19' formation,[7,41] dislocation slip,[7,42] or twinning[7,42–44] depending on the orientation of the parent B2 grains; the extent of which can be increased with increasing strain level.

Returning to the final μ-DIC frame, let us discuss how these deformation mechanisms and the strain distribution impact the reverse transformation of TiNi from B19' to B2. The last μ-DIC frame comes after fracture at 5.9 pct global strain (attributed to a relatively large presence of Ti_2Ni, which is observed to fracture at low strains), when the sample has relaxed to a final strain of 4.2 pct (Figure 2(c)). However, early failure allows observation of the strain relaxation and reverse transformation in this alloy. Expectedly, the mean strain of Ti_2Ni decreases (Figure 2(f1)), which is explained by the elastic unloading (and crack closure) of Ti_2Ni. More interestingly, where β_m + $TiNi_{nano}$ and β_m + $TiNi_{micro}$

Table I. Mean and Standard Deviation of the Local Strain Experienced by Each Phase Mixture as a Function of Increasing Global Strain

Global Strain (pct)	1.3				3.7				4.2 Post-fracture			
Phase Mixture	$TiNi_m$	β_m + $TiNi_{nano}$	β_m + $TiNi_{micro}$	Ti_2Ni	$TiNi_m$	β_m + $TiNi_{nano}$	β_m + $TiNi_{micro}$	Ti_2Ni	$TiNi_m$	β_m + $TiNi_{nano}$	β_m + $TiNi_{micro}$	Ti_2Ni
Mean Phase Strain (pct)	1.37	0.95	0.94	0.93	4.46	3.21	3.50	1.12	4.61	3.92	4.32	0.14
Standard Deviation of Phase Strain (pct)	0.53	0.34	0.45	1.31	1.86	1.36	1.65	2.35	2.20	1.76	2.61	2.20

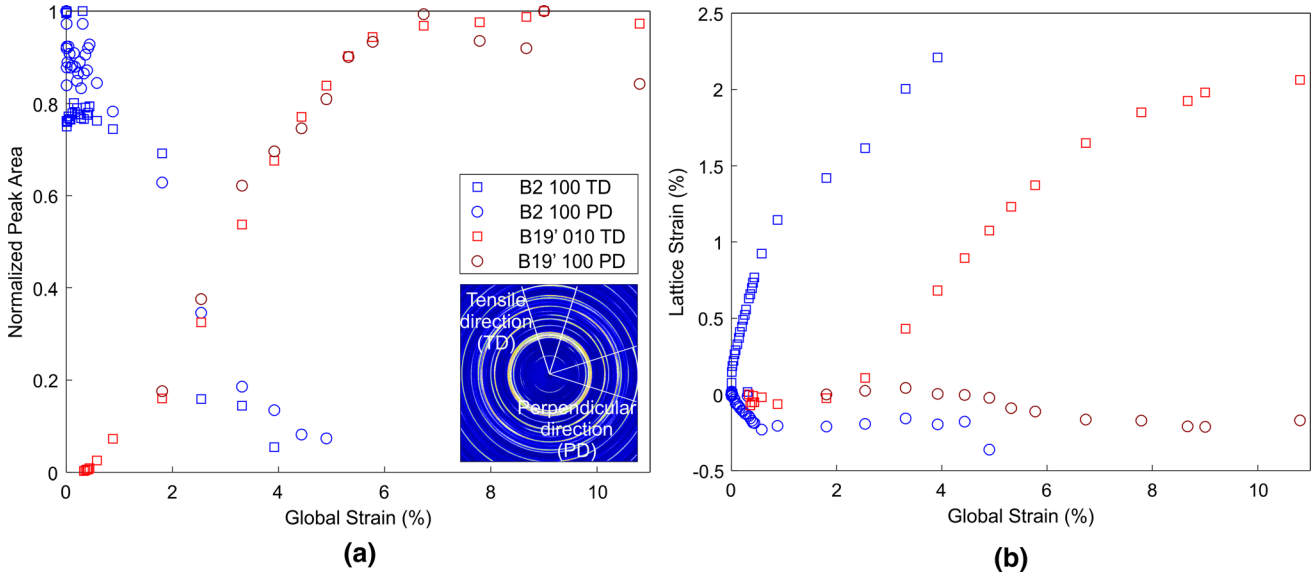

Fig. 3—Synchrotron analysis from the TiNi B2 (100) peaks and B19′ (010) and (100) peaks integrated from 15 deg slices of the tensile direction and perpendicular directions, respectively. (*a*) Peak area normalized by largest measured area measured from same peak. (*b*) Lattice strain development derived from peak shift.

continue to exhibit an increasing local strain, the local strain of $TiNi_m$ only marginally increases (Figure 2(f1)). The change of strain between Figures 2(b) and (c) by each individual facet is mapped in Figure 5(a). This change in strain is due to the multiple contributions: additional plastic deformation and/or forward transformation as the sample is loaded up to fracture (Figure 2(f2-i)), as well as elastic relaxation and reverse transformation after fracture (Figure 2(f2-ii)). The comparatively low average strain increase by $TiNi_m$ is unlikely to be attributed to a lesser contribution during loading, as it has to this point partitioned greater strain. It should then be due to its behavior post-fracture. The elastic strains are small, so the reduced strain exhibited by $TiNi_m$ must largely be due to reverse transformation. In order to confirm this hypothesis, the surface reliefs corresponding to martensitic formation in $TiNi_m$ facets which decrease in strain were inspected. Some of these surface reliefs disappear after fracture, as can be seen by comparing Figures 5(c1) and (c2) and by comparing Figures 5(d1) and (d2). Line profiles drawn across these surface reliefs are provided in Figures 5(c2), (c4), (d2), and (d4), where dark surface reliefs disappear after fracture. Although a greater proportion of $TiNi_m$ facets (38 pct) decrease in strain than β_m + $TiNi_{nano}$ (17 pct) and β_m + $TiNi_{micro}$ (18 pct), this phenomenon occurs in each phase mixture. As observed in our previous work,[11] reverse transformation by the superelastic $TiNi_{nano}$ upon unloading is anticipated. In Figures 5(c1) and (c2), a local contrast change of the β_m grain above the back-transforming $TiNi_m$ is observed in a β_m + $TiNi_{nano}$ region exhibiting decreasing strain, although any contrast change within $TiNi_{nano}$ is unable to be resolved.

What, then, causes fewer β_m + $TiNi_{nano}$ and β_m + $TiNi_{micro}$ facets than $TiNi_m$ facets to exhibit a decrease in strain upon fracture? The most obvious cause is the difference in TiNi phase fraction, as a reduction in TiNi reduces reverse transformation capacity. However, the difference in deformation micro-mechanisms also plays a role. The stress fields from dislocations pinned in β_m at $TiNi_{nano}$ interfaces, as observed in Figures 4(b1) and (b2), are hypothesized to stabilize B19', decreasing the extent of reverse transformation. To probe this hypothesis, we split the facets of each phase mixture into two groups: those which decrease in strain upon final loading and fracture, and those which increase in strain (Figure 5(b)) and compare their strain distributions prior to fracture. For both β_m + $TiNi_{nano}$ and β_m + $TiNi_{micro}$, the higher the pre-existing strain, the less likely the strain is to decrease locally, but for $TiNi_m$, there is a much smaller dependence. Theoretically, the dislocations present in $TiNi_m$ should also stabilize B19′,[45,46] but due to the difference in deformation micro-mechanisms, dislocation locations differ. In grains in which martensitic formation is energetically favored, only few dislocations are expelled during B19′ formation,[47] minimally stabilizing B19′, and slip in neighboring grains should only influence B19′ near the grain boundaries. Thus, despite the higher levels of strain exhibited by $TiNi_m$, there may be less of a stabilizing effect from dislocation plasticity than in β_m + $TiNi_{nano}$ and β_m + $TiNi_{micro}$.

In $V_{45}Ti_{30}Ni_{25}$, the strain-partitioning behaviors by each phase mixture are similar. The differences in phase fraction, morphology, and even deformation micro-mechanisms, which could be expected to cause strain heterogeneities, seem to play a relatively minor role during loading. Instead, the closeness in hardness observed in Figure 1(f) between the phases dominates the differences in deformation micro-mechanisms. This may be compared to materials wherein a large degree of difference in hardness exists, as in model Fe–Ni alloys with both untransformed and reversed austenite[48] or in

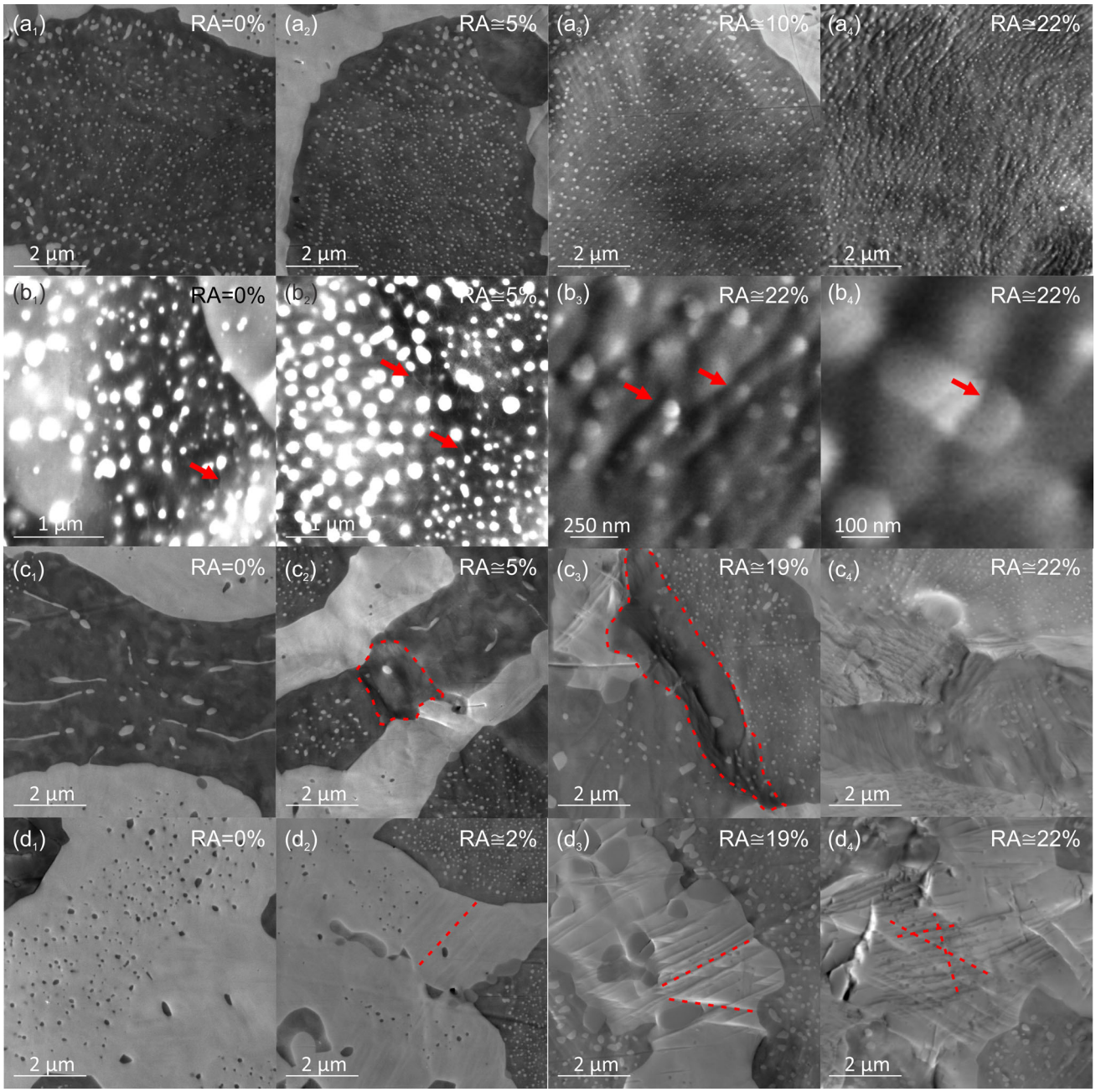

Fig. 4—Post-mortem SE and BSE images from room-temperature tensile test at various local strains, as described by reduction of area (RA). (a_1 to a_4) SE micrographs showing evolution of deformation of β_m + $TiNi_{nano}$. (b_1 to b_2) BSE-ECCI micrographs showing dislocation pinning at $TiNi_{nano}$ in β_m, in 0 pct RA and ~ 5 pct RA regions. (b_3 to b_4) Enlarged SE micrographs from (a_4) showing wavy slip traces avoiding $TiNi_{nano}$ and particle shearing, respectively. (c_1 to c_4) SE micrographs showing evolution of deformation of β_m + $TiNi_{micro}$. (d_1 to d_4) SE micrographs showing evolution of deformation of $TiNi_m$.

bulk metallic glass composites.[16] In those alloys, the phase fraction has a large effect on strain partitioning, as a percolated hard matrix phase imposes cooperative straining between itself and the softer phase, whereas a percolated soft matrix preferentially strains without much deformation of the harder phase. Even when the matrix phase is not percolated, a large difference in hardness of the phases can produce a distinct difference in strain partitioning, as in dual-phase (DP) steels.[49] This also leads to much larger differences in the degree of strain localization. In DP steels, for example, the local strain within strain bands can be six times the median strain.[50] Frequently, these strain bands are located at the phase boundaries and can lead to fracture.[50,51] While the strain bands which do form in $V_{45}Ti_{30}Ni_{25}$ are present primarily in the softer $TiNi_m$ grains and tend to be near phase boundaries with β_m and with Ti_2Ni, the difference between the strains in these bands and outside of them is relatively low as suggested by the closeness in hardness of these phases.

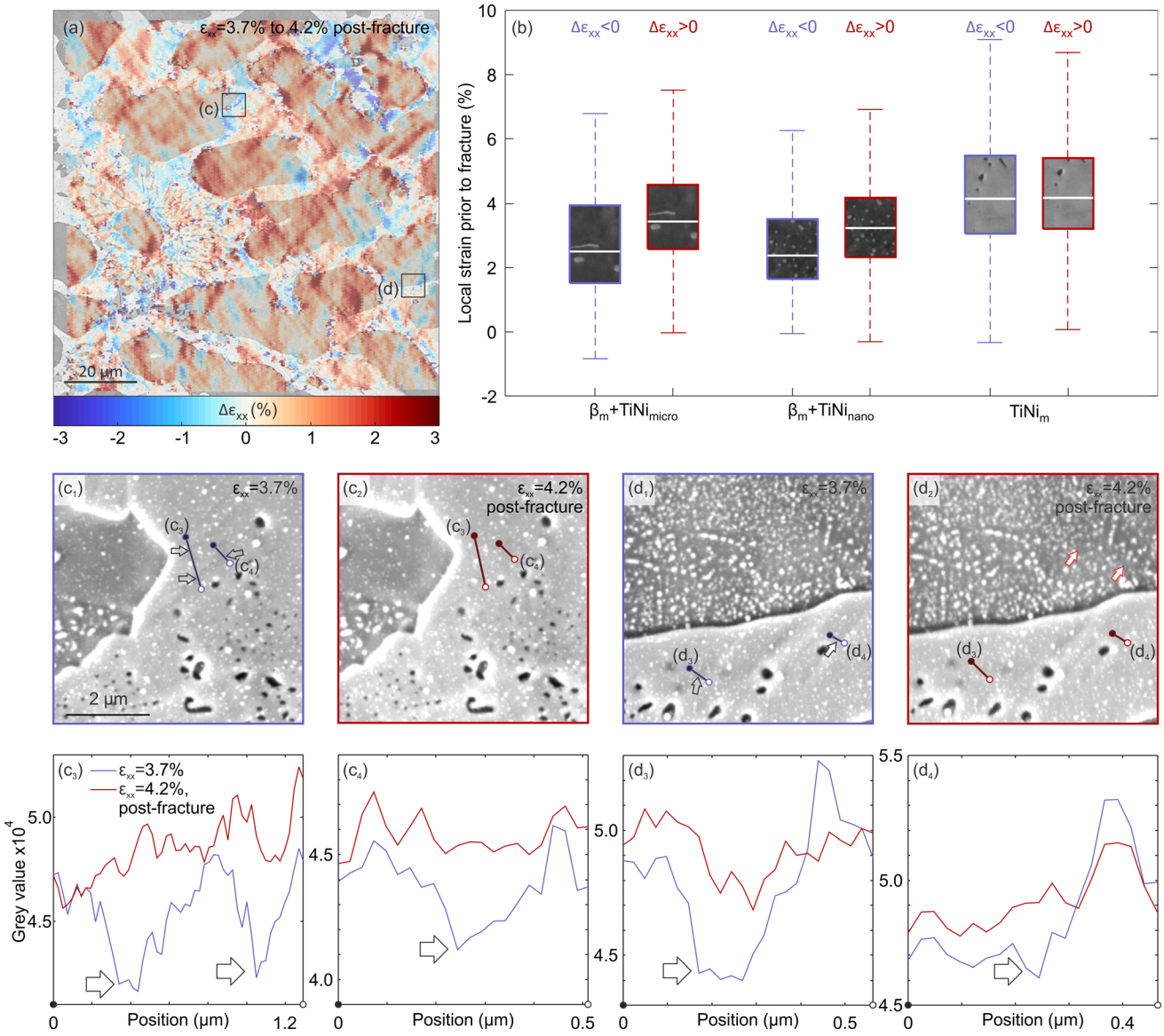

Fig. 5—(*a*) BSE micrograph at a global strain of ε_{xx} = 3.7 pct overlaid with map of the change in local strain after being strained to fracture (ε_{xx} = 5.9 pct) and subsequently relaxing (ε_{xx} = 4.2 pct). (*b*) Box-and-whisker plot comparison of local strains prior to fracture (at a global strain of ε_{xx} = 3.7 pct) between regions in which strains increase ($\Delta\varepsilon_{xx} > 0$) or decrease ($\Delta\varepsilon_{xx} < 0$) upon final straining and fracture for each type of microstructural region. (c_1 to c_2) Pre- and post-fracture SE micrographs, respectively, of a $TiNi_m$ region in which the local strains are relaxed ($\Delta\varepsilon_{xx} < 0$) after final straining and fracture, showing the disappearance of surface contrast associated with martensitic transformation (black arrows). (c_3 to c_4) Gray value line profiles from (c_1 to c_2) showing reduction of surface contrast. (d_1 to d_2) Pre- and post-fracture SE micrographs, respectively, of a $TiNi_m$ region and a β_m + $TiNi_{nano}$ region in which the local strains are relaxed ($\Delta\varepsilon_{xx} < 0$) after final straining and fracture. Contrast change in β_m + $TiNi_{nano}$ is shown with red arrows. (d_3 to d_4) Gray value line profiles from (d_1 to d_2) showing reduction of surface contrast (Color figure online).

Throughout this study on the evolution of deformation of combinations of β and TiNi in various phase mixtures, many similarities and few differences have been observed. However, the differences, though subtle, have large implications. In particular, the dependence of reverse transformation on strain that is observed in β_m + $TiNi_{nano}$ and β_m + $TiNi_{micro}$ answers key questions about the effect of confining superelastic precipitates inside a matrix with close hardness values and provides guidance for future development of multi-phase alloys utilizing transformation-induced crack closure. To enable reverse transformation and prevent consumption of crack closure capability during use, stabilization of the martensitic phase should be avoided by maintaining low strain levels to prevent dislocation pile-up at precipitate boundaries. This is a limitation, as it suggests the application of minimal strains during operations like forming. Alternatively, the stability of the transforming precipitate may be tailored by changing composition or precipitate size, although the moderate size change employed in this alloy did not have a large effect on stability.

The authors would like to thank Jiali Zhang for her contributions. This work was carried out in part through the use of MIT. nano's facilities. We acknowledge the European Synchrotron Radiation Facility for provision of synchrotron radiation facilities, and we would like to thank Andrew Fitch for assistance in using beamline ID22.

FUNDING

Open Access funding provided by the MIT Libraries.

CONFLICT OF INTEREST

On behalf of all authors, the corresponding author states that there is no conflict of interest.

OPEN ACCESS

SUPPLEMENTARY INFORMATION

The online version contains supplementary material available at https://doi.org/10.1007/s11661-022-06900-1.

REFERENCES

1. S. Berveiller, B. Malard, J. Wright, E. Patoor, and G. Geandier: *Acta Mater.*, 2011, vol. 59, pp. 3636–45.
2. H.M. Paranjape, P.P. Paul, H. Sharma, P. Kenesei, J.S. Park, T.W. Duerig, L.C. Brinson, and A.P. Stebner: *J. Mech. Phys. Solids*, 2017, vol. 102, pp. 46–66.
3. A.P. Stebner, H.M. Paranjape, B. Clausen, L.C. Brinson, and A.R. Pelton: *Shape Mem. Superelast.*, 2015, vol. 1, pp. 252–67.
4. A. Bucsek, H. Seiner, H. Simons, C. Yildirim, P. Cook, Y. Chumlyakov, C. Detlefs, and A.P. Stebner: *Acta Mater.*, 2019, vol. 179, pp. 273–86.
5. M. Kimiecik, J.W. Jones, and S. Daly: *Acta Mater.*, 2015, vol. 94, pp. 214–23.
6. H.M. Paranjape, P.P. Paul, B. Amin-Ahmadi, H. Sharma, D. Dale, J.Y.P. Ko, Y.I. Chumlyakov, L.C. Brinson, and A.P. Stebner: *Acta Mater.*, 2018, vol. 144, pp. 748–57.
7. E. Polatidis, M. Šmíd, I. Kuběna, W.-N. Hsu, G. Laplanche, and H. Van Swygenhoven: *Mater. Des.*, 2020, https://doi.org/10.1016/j.matdes.2020.108622.
8. S.M. Ueland and C.A. Schuh: *Acta Mater.*, 2013, vol. 61, pp. 5618–25.
9. H. Hou, E. Simsek, T. Ma, N.S. Johnson, S. Qian, C. Cissé, D. Stasak, N. Al Hasan, L. Zhou, Y. Hwang, R. Radermacher, V.I. Levitas, M.J. Kramer, M.A. Zaeem, A.P. Stebner, R.T. Ott, J. Cui, and I. Takeuchi: *Science*, 2019, vol. 366, pp. 1116–21.
10. R.D. Dar, H. Yan, and Y. Chen: *Scr. Mater.*, 2016, vol. 115, pp. 113–17.
11. J. Zhang, J.L. Cann, S.B. Maisel, K. Qu, E. Plancher, H. Springer, E. Povoden-karadeniz, P. Gao, Y. Ren, B. Grabowski, and C.C. Tasan: *Acta Mater.*, 2020, vol. 196, pp. 710–22.
12. T.M. Adams and J. Mickalonis: *Mater. Lett.*, 2007, vol. 61, pp. 817–20.
13. J. Evtimova, E. Drioli, and G. de Luca: *J. Alloys Compd.*, 2016, vol. 665, pp. 225–30.
14. Z. Mei and J.W. Morris: *Eng. Fract. Mech.*, 1991, vol. 39, pp. 569–73.
15. P. Christel, A. Meunier, M. Heller, J.P. Torre, and C.N. Peille: *J. Biomed. Mater. Res.*, 1989, vol. 23, pp. 45–61.
16. Y. Wu, D. Ma, Q.K. Li, A.D. Stoica, W.L. Song, H. Wang, X.J. Liu, G.M. Stoica, G.Y. Wang, K. An, X.L. Wang, M. Li, and Z.P. Lu: *Acta Mater.*, 2017, vol. 124, pp. 478–88.
17. M. Taira, Y. Nomura, K. Wakasa, M. Yamaki, and A. Matsui: *J. Oral Rehabil.*, 1990, vol. 17, pp. 551–63.
18. H. Jia, G. Wang, S. Chen, Y. Gao, W. Li, and P.K. Liaw: *Prog. Mater. Sci.*, 2018, vol. 98, pp. 168–248.
19. P. Jiang, D. Liang, M. Kellam, G. Song, T. Yuan, W. Wu, and X. Li: *J. Alloys Compd.*, 2017, vol. 728, pp. 63–70.
20. P. Jiang, Y.-D. Yu, G.-S. Song, D. Liang, M. Kellam, and M. Dolan: *Acta Metall. Sin.*, 2015, vol. 28, pp. 15–21.
21. P. Jiang, Y. Yu, G. Song, D. Liang, M. Kellam, and M. Dolan: *Mater. Des.*, 2014, vol. 63, pp. 136–41.
22. B.A. Loomis, L.J. Nowicki, and D.L. Smith: *Fusion React. Mater. Semiannu. Prog. Rep. Period End. March 31,* 1991, pp. 145–55.
23. K. Otsuka and X. Ren: *Prog. Mater. Sci.*, 2005, vol. 50, pp. 511–678.
24. S. Miyazaki, K. Otsuka, and Y. Suzuki: *Scr. Metall.*, 1981, vol. 15, pp. 287–92.
25. X. Tan, D. Ponge, W. Lu, Y. Xu, X. Yang, X. Rao, D. Wu, and D. Raabe: *Acta Mater.*, 2019, vol. 165, pp. 561–76.
26. D. Yan, C.C. Tasan, and D. Raabe: *Acta Mater.*, 2015, vol. 96, pp. 399–409.
27. N. Kamikawa, M. Hirohashi, Y. Sato, E. Chandiran, G. Miyamoto, and T. Furuhara: *ISIJ Int.*, 2015, vol. 55, pp. 1781–90.
28. A. Wanner and D.C. Dunand: *Metall. Mater. Trans. A*, 2000, vol. 31A, pp. 2949–62.
29. D.R. Black, D. Windover, A. Henins, J. Filliben, and J.P. Cline: *Powder Diffr.*, 2011, vol. 26, pp. 155–58.
30. A.P. Hammersley: *ESRF Intern. Report, ESRF97HA02T*, 1997.
31. A.P. Hammersley, S.O. Svensson, M. Hanfland, A.N. Fitch, and D. Häusermann: *High Press. Res.*, 1996, vol. 14, pp. 235–48.
32. Y. Zhang, X. Cheng, and H. Cai: *Mater. Des.*, 2016, vol. 92, pp. 486–93.
33. A. Coda, S. Zilio, D. Norwich, and F. Sczerzenie: *J. Mater. Eng. Perform.*, 2012, vol. 21, pp. 2572–77.
34. A. Toro, F. Zhou, M.H. Wu, W. Van Geertruyden, and W.Z. Misiolek: *J. Mater. Eng. Perform.*, 2009, vol. 18, pp. 448–58.
35. O.V. Kokorev, V.N. Khodorenko, G.A. Baigonakova, E.S. Marchenko, Y.F. Yasenchuk, V. Gunther, S.G. Anikeev, and G.A. Barashkova: *Russ. Phys. J.*, 2019, vol. 61, pp. 1734–40.
36. X. Liu, M. Cao, W. Jin, C. Meng, and D. Yang: *J. Mater. Sci. Technol.*, 2001, vol. 17.
37. M. Ataei, A. Zarei-Hanzaki, and A. Shamsolhodaei: *Mater. Sci. Eng. A*, 2017, vol. 680, pp. 291–96.
38. H. Sehitoglu, I. Karaman, R. Anderson, X. Zhang, K. Gall, H.J. Maier, and Y. Chumlyakov: *Acta Mater.*, 2000, vol. 48, pp. 3311–26.
39. A.H.W. Ngan and M. Wen: *Phys. Rev. Lett.*, 2001, vol. 87, pp. 75505-1–75505-4.

40. A.J. Ardell: *Metall. Trans. A*, 1985, vol. 16, pp. 2131–65.
41. S.C. Mao, J.F. Luo, Z. Zhang, M.H. Wu, Y. Liu, and X.D. Han: *Acta Mater.*, 2010, vol. 58, pp. 3357–66.
42. H. Sehitoglu, Y. Wu, S. Alkan, and E. Ertekin: *Philos. Mag. Lett.*, 2017, vol. 97, pp. 217–28.
43. T. Ezaz, H. Sehitoglu, W. Abuzaid, and H.J. Maier: *Mater. Sci. Eng. A*, 2012, vol. 558, pp. 422–30.
44. L. Heller, P. Šittner, P. Sedlák, H. Seiner, O. Tyc, L. Kadeřávek, P. Sedmák, and M. Vronka: *Int. J. Plast.*, 2019, vol. 116, pp. 232–64.
45. T. Ungár, J. Frenzel, S. Gollerthan, G. Ribárik, L. Balogh, and G. Eggeler: *J. Mater. Res.*, 2017, vol. 32, pp. 4433–42.
46. C. Yu, G. Kang, D. Song, and Q. Kan: *Comput. Mater. Sci.*, 2012, vol. 56, pp. 1–5.
47. J.T. Lim and D.L. Mcdowell: in *Proceedings of SPIE*, 1994, pp. 326–41.
48. N. Nakada, S. Kawasaki, Y. Kogakura, T. Tsuchiyama, and S. Takaki: *Mater. Sci. Eng. A*, 2017, vol. 690, pp. 270–76.
49. Z.H. Cong, N. Jia, X. Sun, Y. Ren, J. Almer, and Y.D. Wang: *Metall. Mater. Trans. A*, 2009, vol. 40A, pp. 1383–87.
50. H.S. Oh, K. Biggs, O. Güvenç, H. Ghassemi-Armaki, N. Pottore, and C.C. Tasan: *Acta Mater.*, 2021, https://doi.org/10.1016/j.actamat.2021.117023.
51. A.C. Darabi, V. Guski, A. Butz, J. Kadkhodapour, and S. Schmauder: *Mech. Mater.*, 2020, vol. 143, p. 103339.